Dalton Transactions

Synthesis and structural characterization of the new Zintl phases Eu10Mn6Bi12 and Yb10Zn6Sb12

Journal:	*Dalton Transactions*
Manuscript ID	DT-ART-06-2022-002011.R1
Article Type:	Paper
Date Submitted by the Author:	04-Aug-2022
Complete List of Authors:	Janzen, Ryan; University of Delaware, Chemistry and Biochemistry Baranets, Sviatoslav; University of Delaware, Chemistry and Biochemistry Bobev, Svilen; University of Delaware, Chemistry and Biochemistry

ARTICLE

Synthesis and structural characterization of the new Zintl phases $Eu_{10}Mn_6Bi_{12}$ and $Yb_{10}Zn_6Sb_{12}$

Received 00th January 20xx,
Accepted 00th January 20xx

DOI: 10.1039/x0xx00000x

Ryan Janzen,[a, #] Sviatoslav Baranets,[a,b #] Svilen Bobev [a,*]

Two new ternary compounds, $Eu_{10}Mn_6Bi_{12}$ and $Yb_{10}Zn_6Sb_{12}$, were synthesized and structurally characterized. The synthesis was achieved either through reactions in sealed niobium tubes or in alumina crucibles by combining the elements in excess molten Sb. Their structures were elucidated using single-crystal X-ray diffraction, and they were determined to crystallize in the orthorhombic space group *Cmmm* (No. 65) with the $Eu_{10}Cd_6Bi_{12}$ structure type. Akin to the archetype phase, both Mn and Zn sites contain about 25% of vacancies. The anionic substructure of the title phases can be described as $[M_6Pn_{12}]$ (*M* = Zn, Mn; *Pn* = Sb, Bi) double layers composed of the corner and edge-sharing $[MPn_4]$ tetrahedra, linked by $[Pn_2]^{4-}$ dumbbells. Eu^{2+}/Yb^{2+} cations fill the space between the layers, with the valence electron counts adhering closely to the Zintl-Klemm rules, i.e., both $Eu_{10}Mn_6Bi_{12}$ and $Yb_{10}Zn_6Sb_{12}$ are expected to be valence-precise compounds. Analysis of the electronic structure and transport properties of $Yb_{10}Zn_6Sb_{12}$ indicate semimetallic behavior with relatively low Seebeck coefficient and resistivity that slightly decreases as a function of temperature.

Introduction

The Zintl concept was formulated in order to explain the complex bonding in a class of polar intermetallic compounds formed by metals with large differences in electronegativity.[1] In such compounds, known as Zintl phases, the bonding can be understood as an ionic interaction in which each atom attains a full octet by donating or accepting valence electrons, with electronegative elements also forming covalent bonds in order to satisfy the octet.[2,3] Such compounds consequentially exhibit properties somewhere between traditional ionic and metallic materials, and thus have a variety of possible applications. Zintl phases appear to be a uniquely promising field for the discovery of new thermoelectric materials, owing to their inherent tunability, and the tendency of structurally complex phases to have unique physical properties and better thermoelectric qualities.[4–7] Specifically, transition-metal Zintl pnictides appear to be an exciting area of research, given the discovery of numerous such phases with unique physical properties.[8–11] Studies on these complex structures have shown a pattern of joined transition-metal-centered tetrahedra $[MPn_4]$ (*M* = Mn, Zn, Cd; *Pn* = P, As, Sb Bi), formed by covalently bonded metal and pnictogen atoms.[12] For instance, $[MnBi_4]$ tetrahedra are seen in such Zintl phases as $AE_9Mn_4Bi_9$[13], $AE_{21}Mn_4Bi_{18}$[14], $AE_{14}MnBi_{11}$[15], $AEMn_2Bi_2$[16], and AE_2MnBi_2[17], whereas $[ZnSb_4]$ tetrahedra are typical building blocks for the structures of $AE_{21}Zn_4Sb_{18}$[18], $AE_{14}ZnSb_{11}$[19], $AE_{10}ZnSb_9$[20], $AE_9Zn_{4+x}Sb_9$[21], and $AEZn_2Sb_2$[22] (*AE* = Ca, Sr, Ba, Eu, Yb), to name a few.

The archetype phase $Eu_{10}Cd_6Bi_{12}$ was previously discovered by our research group and it remained the first and only structure of its kind up until now[23]. Structural analogues of this compounds have been elusive, but a serendipitous discovery yielded $Yb_{10}Zn_6Sb_{12}$; further exploratory work led to the identification of $Eu_{10}Mn_{6+x}Bi_{12}$ ($x \approx 0.4$). Both compositions are abbreviated as $Yb_{10}Zn_6Sb_{12}$ and $Eu_{10}Mn_6Bi_{12}$ throughout the text. At the outset, we draw attention to the fact that $Yb_{10}Zn_6Sb_{12}$ became the fourth known (structurally characterized) phase in the Yb–Zn–Sb compositional diagram in addition to $Yb_{14}ZnSb_{11}$, $Yb_9Zn_{4+x}Sb_9$ and $YbZn_2Sb_2$.[19,21,22] To date, $Eu_{10}Mn_6Bi_{12}$ is the third known phase in the Eu–Mn–Bi system, with the other two being $EuMnBi_2$ and $Eu_{14}MnBi_{11}$.[24-26] The two new crystal structures were elucidated by single-crystal X-ray diffraction methods and were found to fit nicely within the realm of the Zintl-Klemm concept[2,3]. These findings with regards to partitioning the valence electrons are supported by first-principle band-structure calculations. Preliminary transport property measurements were carried out for single-crystalline $Yb_{10}Zn_6Sb_{12}$ (the more air-stable of the two title compounds) in order to explore their potential for the thermoelectric applications.

[a] *Department of Chemistry and Biochemistry, University of Delaware, Newark, Delaware, 19716, United States.*
[b] *Department of Chemistry, Louisiana State University, Baton Rouge, LA 70803, United States*

 # These authors contributed equally

* Corresponding author Email: bobev@udel.edu.

Electronic Supplementary Information (ESI) available: Figures showing cation coordination in $Yb_{10}Zn_6Sb_{12}$, and a structural representation with anisotropic displacement parameters. Results from refinements of the $Eu_{10}Mn_6Bi_{12}$ structure with split Eu1 position. Results from SEM and TG/DSC analysis for $Yb_{10}Zn_6Sb_{12}$. Results from resistivity measurements for single-crystalline $Yb_{10}Zn_6Sb_{12}$. See DOI: 10.1039/x0xx00000x

Experimental

Synthetic procedures

All steps during synthesis were carried out in an argon-filled glove box or under vacuum. All elements were sourced from Alfa or Ames Laboratory with a purity of 99.9 wt.% or higher. $Eu_{10}Mn_6Bi_{12}$ was obtained by loading elements in that precise stoichiometric ratio into a niobium tube, which was weld shut under argon gas and then sealed into an evacuated fused-silica jacket. This silica tube was then placed in a tube furnace and heated. The reaction mixture was brought to 1123 K at a rate of 100 K/hr, allowed to dwell at that temperature for 24 hours, then cooled to 573 K at a rate of 5 K/hr. The silica tube was then cut open using a diamond saw, and the niobium tube brought inside the glove box and opened. What was recovered as products were a few large silvery chunks and many smaller silvery crystals of irregular shapes.

$Yb_{10}Zn_6Sb_{12}$ was obtained by loading elements in a 1:1:3 ratio into an alumina crucible, using an Sb self-flux method, where the Sb acts a "solvent" for the reaction.[27] The alumina crucible was sealed into an evacuated silica jacket, and the resulting ampoule was placed into a muffle furnace for heating. The reaction mixture was brought to 1273 K at a rate of 100 K/hr, allowed to dwell at that temperature for 24 hours, then cooled to 1023 K at a rate of 3 K/hr. The mixture was then centrifugated at high speeds to remove excess molten Sb, and the ampoule was opened inside the glovebox. The product was a variety of phases, with the target phase present as black needles, some of which were of suitable size for the transport properties measurements.

Analogous reactions with Ca and Sr failed to produce isostructural phases.

Table 1. Selected single-crystal data and structure refinement parameters for $Eu_{10}Mn_6Bi_{12}$ and $Yb_{10}Zn_6Sb_{12}$.

CCSD number	2178400	2178399
Empirical formula	$Eu_{10}Mn_{6.47(2)}Bi_{12}$	$Yb_{10}Zn_6Sb_{12}$
Formula weight (g/mol)	4382.82	3583.62
Temperature (K)	200	
Radiation (λ)	Mo $K\alpha$, 0.71073 Å	
Crystal system	Orthorhombic	
Space group, Z	*Cmmm* (No. 65), 1	
a (Å)	7.798(3)	7.2712(6)
b (Å)	23.903(9)	22.7869(18)
c (Å)	4.7623(17)	4.5046(4)
V (Å^3)	887.7(6)	746.36(11)
ρ_{calc} (g/cm^3)	8.20	7.97
μ (cm^{-1})	787.6	463.0
Goodness-of-fit on F^2	1.039	1.159
R_1 ($I \geq 2\sigma_I$)[a]	0.0353	0.0250
wR_2 ($I \geq 2\sigma_I$)[a]	0.0637	0.0545
Largest diff. peak/hole (e$^-$/ Å^{-3})	2.37/–2.20	1.53/–2.27

[a] $R_1 = \sum||F_o|-|F_c||/\sum|F_o|$; $wR_2 = [\sum[w(F_o^2-F_c^2)^2]/\sum[w(F_o^2)^2]]^{1/2}$, where $w = 1/[\sigma^2F_o^2 + (AP)^2 + (BP)]$ and $P = (F_o^2 + 2F_c^2)/3$; where A and B are weight coefficients (see CIF).

Crystallography

Powder X-ray diffraction. The samples for powder X-ray diffraction (PXRD) were prepared inside of an argon-filled glovebox to prevent oxidation, and all measurements were performed inside of a nitrogen-filled glovebox for the same reason. The powder diffraction patterns were collected at room temperature on a Rigaku MiniFlex powder diffractometer using filtered Cu $K\alpha$ radiation (λ = 1.5418 Å). The data were collected between 5 and 75° in 2θ with a step size of 0.05° and 2s/step counting time. Analysis was carried out with the JADE 6.5 software package, and the peak positions and intensities were in good agreement with those calculated based on refined crystal structures.

Single-crystal X-ray diffraction. Single-crystal X-ray diffraction (SCXRD) data were collected on a Bruker APEX-II CCD diffractometer equipped with a Mo $K\alpha$ (λ = 0.71073 Å) source. Single crystals of the title phases were selected and cut to appropriate dimensions in Paratone-N oil. The crystals were quickly transferred to the goniometer for measurement, with the temperature held at 200 K for the duration of the experiment using a stream of cold nitrogen gas. Data acquisition was performed with the Bruker-supplied software.[28] Multi-scan absorption correction was applied using SADABS software.[29] The structure solution and refinements were done using ShelXT and ShelXL through the Olex2 graphical interface.[30–32] Atomic coordinates were standardized using the STRUCTURE TIDY program.[33] Selected details of the data collection and relevant crystallographic parameters are given in Tables 1–2. CCDC deposition numbers 2178399 and 2178400 contain the full supplementary crystallographic data for the two compounds discussed in this paper. CIF can be obtained free of charge via www.ccdc.cam.ac.uk/data_ request/cif, or by emailing data_request@ccdc.cam.ac.uk, or by contacting The Cambridge Crystallographic Data Centre, 12 Union Road, Cambridge CB2 1EZ, U.K., fax +44 1223 336033.

Thermopower and electrical resistivity measurements

Seebeck coefficient data sets were collected for single-crystals of $Yb_{10}Zn_6Sb_{12}$, using the integral method, and utilizing constantan wire as a reference material. As-grown crystals of suitable size were used. The crystals were mounted and connected the probe using high purity silver conductive paint obtained from SPI Supplies. The samples were then inserted into a temperature-variable chamber from MMR Tech. and evacuated to ca. 10 mTorr once the paint was sufficiently dry. The data were collected utilizing the SB-100 module within a temperature window of 300–600 K with a step of 20 K. The data were collected during both heating and cooling cycles to ensure reproducibility. Electrical resistivity data was also collected for $Yb_{10}Zn_6Sb_{12}$ using the MMR Tech. setup. The crystal was connected to the system using 4 platinum wires adhered to the surface of the crystal with silver conductive paint. Measurements were taken in the interval from 300–450 K with increments of 10 K.

The $Eu_{10}Mn_6Bi_{12}$ samples proved to be unsuitable for measurements, as elaborated below.

Table 2. Atomic coordinates and equivalent displacement parameters U_{eq} (Å^2) for $Eu_{10}Mn_6Bi_{12}$ and $Yb_{10}Zn_6Sb_{12}$.

Atom	Wyckoff	*x*	*y*	*z*	U_{eq}[a]
		$Eu_{10}Mn_6Bi_{12}$			
Eu1	4*i*	0	0.41525(7)	0	0.035(1)
Eu2	4*e*	¼	¼	0	0.021(1)
Eu3	2*a*	0	0	0	0.021(1)
Mn[b]	8*q*	0.1893(5)	0.11766(2)	½	0.023(1)
Bi1	4*j*	0	0.31444(5)	½	0.020(1)
Bi2	4*i*	0	0.13755(4)	0	0.022(1)
Bi3	4*h*	0.29271(2)	0	½	0.022(1)
		$Yb_{10}Zn_6Sb_{12}$			
Yb1[c]	8*p*	0.0253(5)	0.41228(3)	0	0.018(1)
Yb2	4*e*	¼	¼	0	0.015(2)
Yb3	2*a*	0	0	0	0.012(2)
Zn[c]	8*q*	0.1938(2)	0.11826(8)	½	0.023(1)
Sb1	4*j*	0	0.31235(4)	½	0.012(1)
Sb2	4*i*	0	0.13679(4)	0	0.018(1)
Sb3	4*h*	0.29950(1)	0	½	0.012(2)

[a] U_{eq} is defined as one third of the trace of the orthogonalized U_{ij} tensor.
[b] Refined site occupancy factor (SOF) is 0.809(10).
[c] Constrained SOFs: 50% for Yb1 site, 75% for Zn site.

Elemental analysis

Energy-dispersive X-ray spectroscopy (EDS) analysis was performed on an Auriga 60 CrossBeam Scanning Electron Microscope equipped with an Oxford Synergy X-MAX80 detector and an EDSD detector. Point analysis was performed on the crystals, and data were collected from several spots for each measured single crystal. The obtained quantitative chemical compositions were in good agreement with the SCXRD refinements, with the observed deviations within the error limitations of the technique.

Thermal analysis

Simultaneous thermogravimetric and differential scanning calorimetry (TG/DSC) measurements were performed on ca. 17 mg of the $Yb_{10}Zn_6Sb_{12}$ sample using an SDT Q600 analyzer, supplied by TA Instruments. The sample was loaded in a capped alumina pan. After equilibration at 323 K, the temperature was increased to 1223 K at a rate of 20 K/min. The sample was held at this point for 1 min and then cooled to 373 K at a rate of 20 K/min. To prevent oxidation, the measurements were performed under a constant flow (100 mL/min) of high purity argon.

Electronic structure calculations

Electronic structure calculations were performed on fully stoichiometric and devoid of disorder $Yb_{10}Zn_8Sb_{12}$, in the density functional theory framework using the TB-LMTO-ASA code.[34] The difference between the presented and refined composition originates from the occupancy of Zn site (Table 2). Due to the limitations of the TB-LMTO code, fully occupied atomic sites must be considered for the electronic structure calculations. An introduction of empty spheres was necessary to satisfy the atomic sphere approximations. The von Barth-Hedin implementation of the local density approximation was used.[35] The density of states and band structures were calculated after convergence of the total energy on the *k*-mesh with 8 x 4 x 25 points in the Brillouin zone. The Fermi level was selected as the energy reference (E_F = 0 eV). The experimental unit cell parameters and atomic coordinates for $Yb_{10}Zn_6Sb_{12}$, as displayed in Tables 1 and 2, were used for setting up the calculations. The basis set included 6s, 6p, 5d and 4f orbitals for Yb, 4s, 4p, and 3d orbitals for Zn, and 5s, 5p, and 5d orbitals for Sb.

We also computed the band structure of the hypothetical and yet to be discovered analogue $Ca_{10}Zn_8Sb_{12}$, where Ca substituted for Yb. This was done with the goal to ease the calculations by excluding the 4f orbitals from a consideration.

The Ca 4p, Yb 6p, and Sb 5d orbitals were treated with downfolding techniques. The COHP method was used to perform bonding analysis.[36]

Results and discussions

Synthesis

The $Eu_{10}Mn_6Bi_{12}$ phase was discovered while searching for analogs to the Zintl phase $Eu_{10}Cd_6Bi_{12}$ in the Eu–Mn–Bi system. The products of the reactions we run were not phase pure—besides $Eu_{10}Mn_6Bi_{12}$, there were also significant amounts of $EuMnBi_2$ and traces of another, yet unidentified phase. Attempts to achieve the same product with Bi-flux, Pb-flux, and Sn-flux reactions all failed, producing either $EuMnBi_2$ or binary phases containing the flux elements. An analogous reaction with Zn did not produce an isostructural phase.

The inability to obtain single-crystals via the flux method and the phase purity issues with direct reactions (note that they did not yield large crystals, suitable for bulk materials properties characterization) rendered the measurements of the properties of the phase impossible. We must also add here that even if one manages to grow large enough crystals, or obtain phase-pure polycrystalline sample of $Eu_{10}Mn_6Bi_{12}$, extra care need to be taken in handling the material since it quickly deteriorates when exposed to air.

In opposite to the $Eu_{10}Mn_6Bi_{12}$ phase, $Yb_{10}Zn_6Sb_{12}$ appears to be relatively more air stable compared to $Eu_{10}Mn_6Bi_{12}$, Another noteworthy difference between the two samples was that $Yb_{10}Zn_6Sb_{12}$ can be synthesized using antimony as a reactive solvent, despite the known challenges for the flux separation (melting point of Sb is ca. 904 K). The Sb flux technique has been successfully implemented for the synthesis of many antimonides, many of which are promising thermoelectric materials, such as Mg_3Sb_2, $YbMnSb_2$, and $A_{10}MSb_9$ (*A* = Ca, Yb; *M* = Zn, Mn, Ga, In).[20,37-40] In this regard, we must note that many nominal compositions were tried (including attempting to synthesize $YbZnSb_2$ and $Yb_{10}ZnSb_9$ as isostructural analogs of $YbMnSb_2$ and $Yb_{10}MnSb_9$), yet, all reactions produced large plate-like crystals of $YbZn_2Sb_2$[22] as the

major product, and only a small amount of needles that were later identified as the title phase. Optimization attempts failed to produce phase-pure products. However, since the two phases have easily distinguishable morphologies, we were able to extract enough $Yb_{10}Zn_6Sb_{12}$ material to study its transport properties.

Crystal structure

$Yb_{10}Zn_6Sb_{12}$ and $Eu_{10}Mn_6Bi_{12}$ crystallize in the orthorhombic space group *Cmmm* (No. 65). They belong to the $Eu_{10}Cd_6Bi_{12}$ structure type.[23] The basic structure contains 7 independent sites in the asymmetric unit (Table 2). There are some subtleties concerning both structures and at the outset, we must note that the Yb-bearing phase shows more intricate disordered. Therefore, we start our discussion with a brief description of the $Eu_{10}Mn_6Bi_{12}$ phase ($Eu_{10}Mn_{6+x}Bi_{12}$ phase, in actuality).

The $Eu_{10}Mn_6Bi_{12}$ structure is identical to that of the $Eu_{10}Cd_6Bi_{12}$ archetype, boasting an anionic substructure, which can be described as double layers (formally $[Mn_6Bi_{12}]$) that are stacked along the *b* axis in an *ABAB* sequence, as shown in Figure 1. The layers are comprised of $[MnBi_4]$ tetrahedra, which share common corners and edges. While these slabs form the anionic portion of the structure, the remaining Eu cations occupy the spaces between and within the tetrahedra at optimal packing density for the amount necessary to balance the total charge on the anions. The voids left in the polyanionic structure resemble infinitely long channels in octagonal and double-pentagonal shapes oriented along the *c*-axis. The double-pentagonal channels are noteworthy because corners of $[MnBi_4]$ tetrahedra are connected through homoatomic Bi–Bi bonds, akin to the structural units previously observed in some structurally and compositionally similar Zintl pnictides (Figure 1) such as $AE_{11}M_6Sb_{12}$ (*AE* = Ba, Eu; *M* = Zn, Cd) and $Eu_{10}Mn_6Sb_{13}$.[41–43]

The Bi–Bi bond in $Eu_{10}Mn_6Bi_{12}$ measures 3.23 Å long (Table 3). This value is longer than the double of the approximate covalent radius of Bi, 3.02 Å,[44] and also slightly longer than the observed distance of 3.15 Å in $Eu_{10}Cd_6Bi_{12}$,[23] yet comparable to the multi-centered Bi–Bi bonds in the $Ca_{14}AlBi_{11}$ structure and its derivatives.[45]

Table 3. Selected interatomic distances in $Eu_{10}Mn_{6+x}Bi_{12}$ and $Yb_{10}Zn_6Sb_{12}$.

Atom Pair	Distance (Å)	Atom Pair	Distance (Å)
$Eu_{10}Mn_6Bi_{12}$			
Eu1–Bi1 x2	3.388(2)	Mn–Bi1	2.916(4)
Eu1–Bi3 x4	3.519(1)	Mn–Bi2 x2	2.842(2)
Eu2–Bi1 x4	3.4414(9)	Mn–Bi3	2.926(4)
Eu2–Bi2 x2	3.320(1)	Bi3–Bi3	3.233(3)
Eu3–Bi2 x2	3.288(2)		
Eu3–Bi3 x4	3.298(1)		
$Yb_{10}Zn_6Sb_{12}$			
Yb1–Sb1 x2	3.2082(9)	Zn–Sb1	2.731(2)
Yb1–Sb3 x4	3.270(1)	Zn–Sb2 x2	2.6903(9)
Yb2–Sb1 x4	3.2242(4)	Zn–Sb3	2.802(2)
Yb2–Sb2 x2	3.1558(7)	Sb3–Sb3	2.916(2)
Yb3–Sb2 x2	3.1171(9)		
Yb3–Sb3 x4	3.1329(6)		

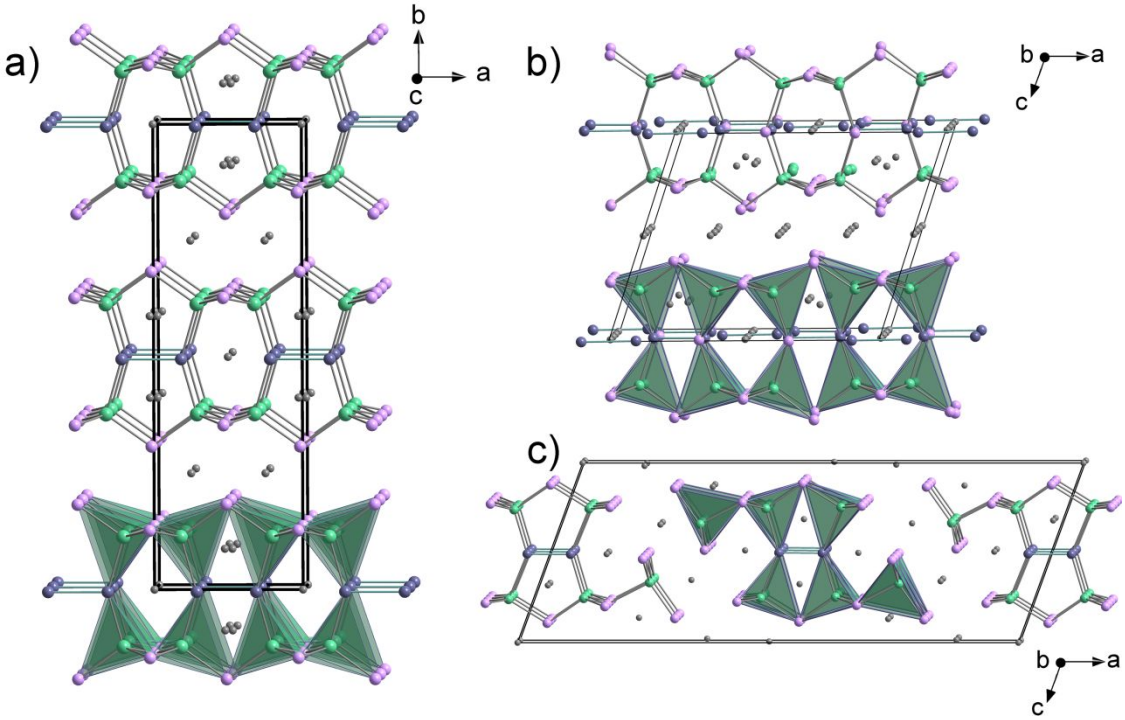

Figure 1. (a) Crystal structure of $Eu_{10}Mn_6Bi_{12}$, viewed down the *c*-axis with unit cell outlined (space group *Cmmm*). The Bi atoms are shown as purple spheres; the ones shown in darker shades (in all panels) are dimerized. The Bi atoms are all located on the vertices of Mn-centered tetrahedra, which are represented in green. The Eu cations are shown as small grey spheres between the polyanions. (b) Crystal structure of $Eu_{10}Mn_6Sb_{13}$, viewed down the *b*-axis (space group *C*2/*m*). Here, the color code is the same as in (a) with the dark purple spheres representing the "extra" antimony atoms. (c) Crystal structure of the other, compositionally and structurally similar "11-6-12" phase (archetype $Sr_{11}Cd_6Sb_{12}$), viewed down the *b*-axis (space group *C*2/*m*).

ARTICLE

The previously mentioned disorder in $Eu_{10}Mn_6Bi_{12}$ is with regards to the site occupation factor of the single Mn site. Although we simplified the chemical formula as $Eu_{10}Mn_6Bi_{12}$, the reader should be reminded that the structural refinements on several crystals from independent batches yielded $Eu_{10}Mn_{6+x}Bi_{12}$ ($x \approx 0.3$–0.6). Here, we provide two structural datasets findings with Mn site occupation factors at 81% and 79%. The root-cause for the existence of defects on the Mn site is, apparently, the electronically unfavorable "richness" for the fully stoichiometric $Eu_{10}Mn_8Bi_{12}$, while $Eu_{10}Mn_6Bi_{12}$ with ¼ of the Mb atoms missing is electron-balanced (*vide infra*).

Since there are no measurable reflections that violate the global symmetry, we can argue that the Mn-defects are random in nature. In Figure 2, we depict several possible interpretations of $[Mn_6Bi_{12}]$ fragments where ¼ of the Mn atoms are judiciously removed, either from a single slab or a double slab. The similarities between one of these hypothetical motifs with ¼ of the Mn missing (bottom of Figure 2), and the actual ribbon fragment from the "11-6-12" structure (Figure 1c) cannot be overstated. Clearly, the addition of one extra cation and the concomitant cleavage of one of the Bi_2-dimers is what Nature has found as a solution to the packing problem of $[Mn_6Bi_{12}]$ fragments with ordered Mn defects and "spectator" cations.

$Yb_{10}Zn_6Sb_{12}$ has a near-identical structure featuring $[Zn_6Sb_{12}]$ layers and $[ZnSb_4]$ tetrahedra, but there is some additional disorder involving the Yb cations, as shown in Figure S1. Specifically, the significant elongation of the Yb1 thermal parameter (U_{11} was ca. 8 times larger than U_{22}) suggested the possibility for a small positional disorder on this 4*i* site. By splitting this position to two 50% occupied 8*p* Wyckoff sites (approx. 0.4 Å apart), the shape of the ellipsoids was vastly improved. The 50% occupancy indicates the presence of only one Yb atom in the given position at a given time. In addition, the residual features on the difference Fourier map were decreased two-fold and the conventional *R*-factors were lowered. By comparison, in the $Eu_{10}Mn_6Bi_{12}$ structure, the Eu1 anisotropic displacement parameter is much more uniform (U_{11} is ca. 2.5 times larger than U_{22}) and attempts to refine a similar model with split Eu1 on two 8*p* Wyckoff sites did not yield statistically significant improvements.

Two other structural metrics deserve a brief special mention too. First, the Sb–Sb distance within the $[Sb_2]^{4-}$ dimer was refined as 2.916 Å, in good agreement with correspondent distances in similar structures, such as the 2.95 Å observed in $Eu_{10}Mn_6Sb_{13}$.[41] Second, the refined occupancy of Zn site was within 1-2σ from 75%, therefore it was constrained to this value and not treated as a variable. The resultant final formula is $Yb_{10}Zn_6Sb_{12}$ (formula with fully occupied Zn would be $Yb_{10}Zn_8Sb_{12}$).

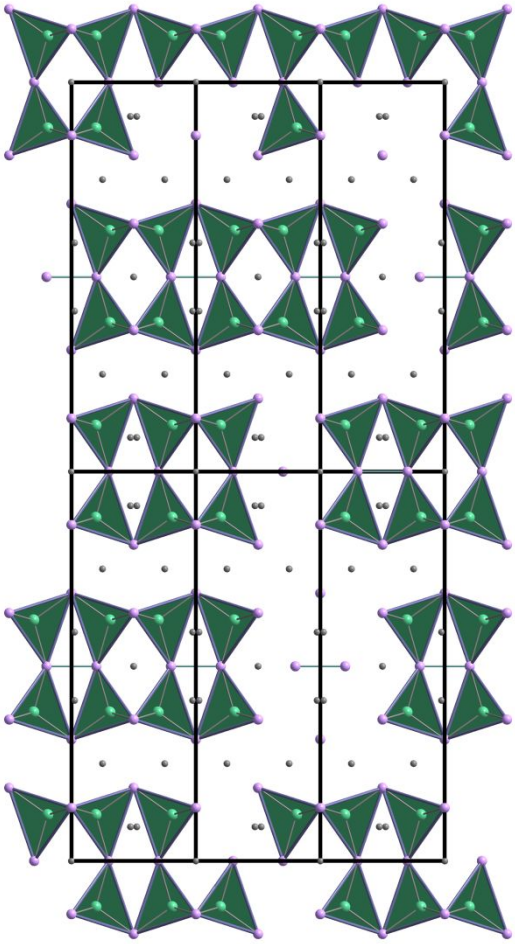

Figure 2. Representation of some possible polyanionic fragments with ¼ of Mn removed from each unit cell.

One may recall that the final formula for the earlier discussed Eu-compound was given as $Eu_{10}Mn_{6+x}Bi_{12}$ ($x \approx 0.3$–0.6). The reason(s) for the small difference between the refinements is not understood at present. One can speculate that the synthetic procedure in Nb tubes may lead to the incorporation of small amounts of Nb into $Eu_{10}Mn_6Bi_{12}$, making the refined occupancy of the Mn site appear as 79–81% (*vide supra*). Nb tubes are known to be "imperfect" reaction vessels for elemental mixtures containing As and Sb, as the latter react with Nb.[46] Bismuth, compared to the lighter group 15 congeners is far less susceptible to form compounds with Nb, nonetheless, this conjecture requires a more detailed follow up investigation.

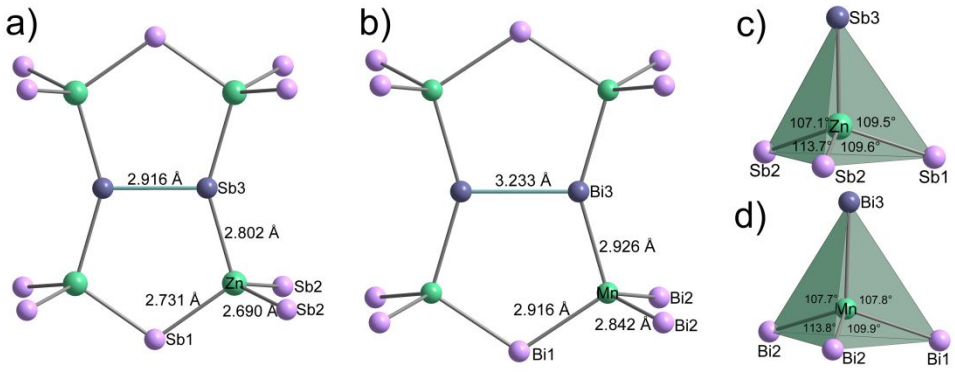

Figure 3. Close up views of the anionic fragments of $Yb_{10}Zn_6Sb_{12}$ (a) and $Eu_{10}Mn_6Bi_{12}$ (b), with bond lengths labeled. Representations of $[ZnSb_4]$ (c) and $[MnBi_4]$ (d) tetrahedra, with corresponding bond angles.

The transition-metal-centered tetrahedra (Figure 3) that form the basic building blocks of these structures display seemingly strong covalent bonding, agreeing with other similar structures.[21,23] The Mn–Bi atomic distances are in the range of 2.84 to 2.92 Å, and thus fit the sum of the Pauling metallic radii well.[47] They agree with other structures containing $[MnBi_4]$ tetrahedra, with the shortest bonds, Mn–Bi2, being comparable to the Mn–Bi bond in $Eu_{14}MnBi_{11}$[26], and $Ca_{14}MnBi_{11}$[48], and the longer bonds being comparable to those in $Ca_{21}Mn_4Bi_{18}$.[14] The Zn–Sb distances are in the range of 2.69 to 2.80 Å (Table 3), and thus also fit the sum of the Pauling metallic radii very well. The bond lengths are comparable to those in other structures containing $[ZnSb_4]$ tetrahedra, as in $Eu_{21}Zn_4Sb_{18}$[18] and $YbZn_2Sb_2$[22] , but are even shorter, especially in the two Zn–Sb2 bonds, indicating strong bonding, as indicative from the electronic structure calculations, vide infra.

Electron count and electronic structure

The Zintl formalism holds true for $Eu_{10}Mn_6Bi_{12}$ and $Yb_{10}Zn_6Sb_{12}$ which both can be rationalized as charge-balanced phases. Keeping in mind the presence of homoatomic pnictogen-pnictogen bonds in form of antimony, $[Sb_2]^{4-}$, or bismuth, $[Bi_2]^{4-}$, dumbbells, the electron balance of the "10-6-12" composition with 75% occupancy of central metal satisfy the valence rules and the following formula breakdown can be suggested: $(AE^{2+})_{10}(M^{2+})_6(Pn^{3-})_8([Pn_2]^{4-})_2$ where *AE* = Eu, Yb; *M* = Mn, Zn; *Pn* = Sb, Bi. Such electron-balanced compositions result from the ¼-deficiency on the *M* site. If the Mn or Zn atom in either structure are fully-occupied, according to the notation $(AE^{2+})_{10}(M^{2+})_8(Pn^{3-})_8([Pn_2]^{4-})_2(e^-)_4$, where e^- stands for an electron, the structures would be electron-rich.

Discussing the basic valence electron count, we need to be cognizant that the final refined composition of the Yb-bearing phase is in fact with the ideal "10-6-12" stoichiometry, whereas $Eu_{10}Mn_{6.47}Bi_{12}$ is slightly deviating from it. Based on that, one should expect that the Yb-compound is charge-balanced, and the Eu-compound is, to some extent, electron-rich.

To better understand the full electronic structure of the title phases, self-consistent first-principle calculations were performed, using fully stoichiometric $Yb_{10}Zn_8Sb_{12}$ composition as a model. Figure 4 shows the calculated total and partial density of states (DOS), band structure diagram, and the Crystal Orbital Hamilton Population (COHPs) of the key bonding interactions in the phase. In the COHP plot, the positive and negative signs represent the bonding and antibonding states, respectively. Self-consistent calculations could not be achieved when treating the Yb 4f orbitals, whose contributions appear just below the Fermi level (E_F = 0 eV) at the valence band maximum (VBM) as a large peak.

The Fermi level itself appears to fall in an area with relatively high DOS and strong antibonding character of Zn–Sb and Sb–Sb interactions, as can be seen from the COHP curves. An area of high DOS at the Fermi level suggests that the electronic structure is not optimized for the "10-8-12" composition, which corresponds to a structure where the Zn site is 100% occupied. The previously mentioned valence electron count is consistent with that notion too, both indicating that partial occupancy of Zn is necessary for electronic stability.

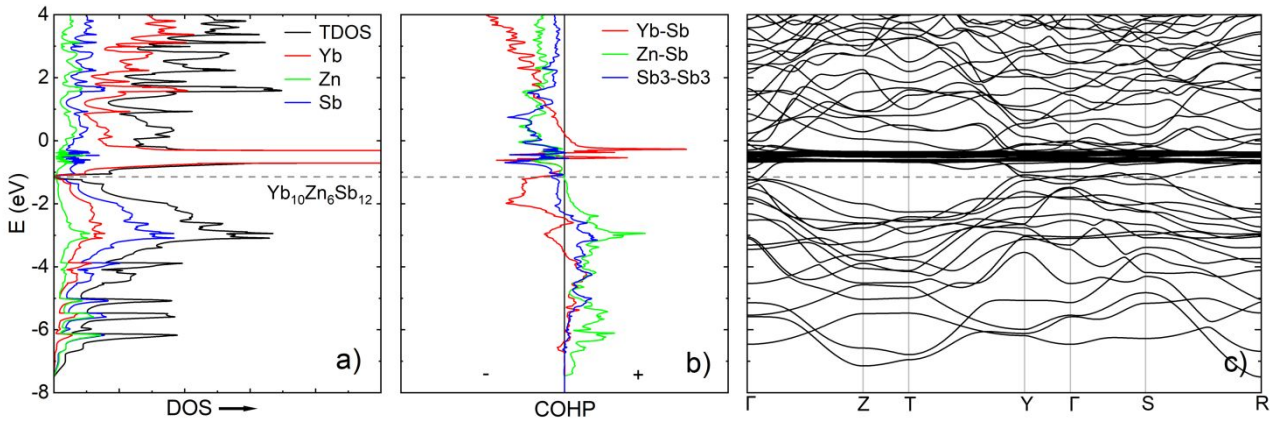

Figure 4. (a) Total density of states of idealized $Yb_{10}Zn_8Sb_{12}$ together with the partial density of states for Yb, Zn, and Sb; (b) calculated COHP diagram for Yb–Sb, Zn–Sb, and Sb3–Sb3 interactions within it; and (c) the calculated bulk electronic band structure of the phase. The pseudogap is 4 electrons away from the Fermi level, set at 0 eV. The "corrected" Fermi level corresponding to the electronically more favorable structure (i.e., $Yb_{10}Zn_6Sb_{12}$) is indicated by the gray dashed line through the graphs. In the COHP plot, the regions indicated by the signs "+" and "-"correspond to the bonding and anti-bonding interactions, respectively.

If two Zn atoms per formula unit are removed, then, the total number of valence electrons in the system decreases to 92, and the Fermi level shifts downward by –1.15 eV (Figure 4). This "corrected" Fermi level is shown on the figure by the gray dashed line. This treatment seems to greatly stabilize the system, as the Fermi level now falls in a pseudogap, with minimal DOS and nearly optimized bonding character of Yb–Sb, Zn–Sb, and Sb–Sb interaction. Among them, some Yb–Sb contacts may be seen as slightly underoptimized, which may be related to the untrue packing assumed for the ordered "10-8-12" model. More appropriate calculations will require a super-structure "10-6-12" model, which may lead to bonding optimization.

To eliminate problems arising from the contribution of the 4f orbitals in $Yb_{10}Zn_8Sb_{12}$, we also performed calculations on a model $Ca_{10}Zn_8Sb_{12}$, employing the same unit cell parameters and atomic coordinates as in $Yb_{10}Zn_8Sb_{12}$ (i.e., without any structural relaxation). Figure 5 shows the calculated total and partial density of states (DOS), band structure diagram, and the Crystal Orbital Hamilton Populations (COHPs) curves of the key bonding interactions in the studied phase. While our attempts to synthesize $Ca_{10}Zn_6Sb_{12}$ were unsuccessful, the similarity of the ionic radii of Yb^{2+} and Ca^{2+} and the existence of multiple isostructural Ca- and Yb-bearing Zintl phases[19,21,22] suggest a reasonableness of such model. Similar to the $Yb_{10}Zn_8Sb_{12}$ model, electronic states above the Fermi level have a predominantly Ca-d character, which is typical for the Zintl phases. Once again, strong antibonding character of Zn–Sb and Sb–Sb interactions is evident at the original Fermi level (Figure 5). Integrating the DOS to 92 total valence electrons leads to a "correction" of the Fermi level, which is shifted downward by –1.69 eV. As before, the Fermi level for the "10-6-12" composition falls in a pseudogap.

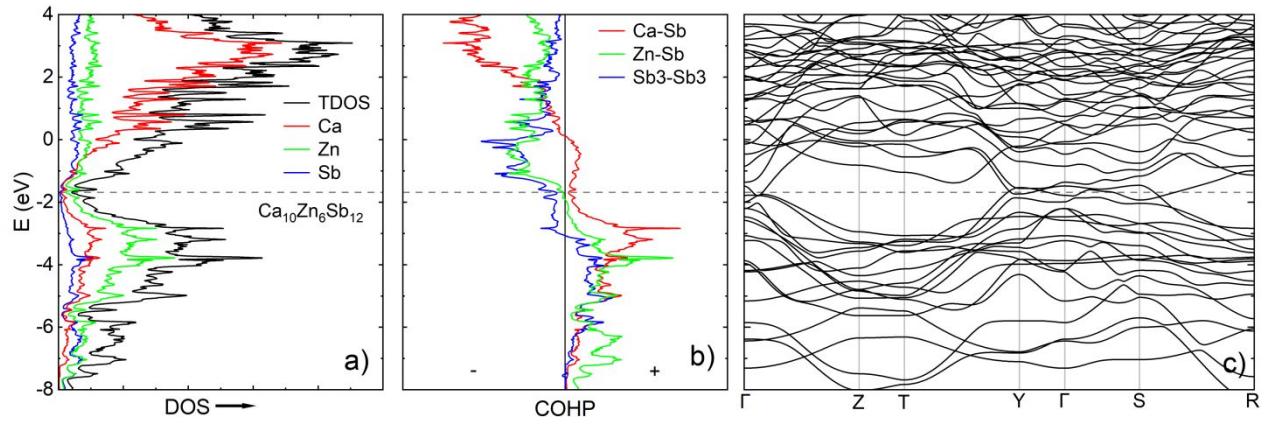

Figure 5. (a) Total density of states of idealized $Ca_{10}Zn_8Sb_{12}$ together with the partial density of states for Ca, Zn, and Sb; (b) calculated COHP diagram for Ca–Sb, Zn–Sb, and Sb–Sb3 interactions within it; and (c) the calculated bulk electronic band structure of the phase. The pseudogap is 4 electrons away from the Fermi level, set at 0 eV. The "corrected" Fermi level corresponding to the electronically more favorable structure (i.e., $Ca_{10}Zn_6Sb_{12}$) is indicated by the gray dashed line through the graphs. In the COHP plot, the regions indicated by the signs "+" and "-"correspond to the bonding and anti-bonding interactions, respectively

As expected for the Zintl antimonides, contributions from Sb-p orbitals are dominant in the valence band below the adjusted Fermi level. At the same energy, Ca–Sb and Zn–Sb contacts are nearly optimized, whereas homoatomic Sb–Sb interactions are slightly underoptimized, showing antibonding state at –1.69 eV. In the extended energy range higher than ca. –3 eV, there is evidence of the strongly π*-antibonding Sb–Sb interactions, again, typical for the Zintl pnictides with homoatomic pnictogen-pnictogen bonding. As a result, beyond minor Ca–Sb bonding interactions above the adjusted Fermi level, there is no space for electronic optimization—more electrons appear to have a destabilizing effect. A follow up advanced calculations of this material are necessary to shed the light on this problem. Regardless, the electronic structure calculations seem to support the rationalization of the title compounds as Zintl phases, though Ca in the hypothetical $Ca_{10}Zn_6Sb_{12}$ does not show perfectly ionic behavior.

Thermal stability and transport properties

Property measurements were conducted only for single-crystalline samples of $Yb_{10}Zn_6Sb_{12}$, as was discussed in the synthetic section. While many Zintl phases were proven to be highly suitable for the high temperature thermoelectric applications[4], our goal was to test a suitability of the title "10-6-12" phases for these purposes. Therefore, we performed a TG/DSC measurement on $Yb_{10}Zn_6Sb_{12}$ to check the thermal stability. As it is evident from Figure S3, no significant weight loss or thermal events occur until past 800 K. Thus, the phase ought to be thermally stable at least up to that point, and transport properties measurements could be reliably run up to that temperature. Past 1000 K, the sample decomposed, eventually losing a noticeable amount of its original mass. A complete deterioration was proved by the collected X-ray powder diffraction pattern, indicating no peaks of the starting phase in the sample post-heating.

Seebeck coefficient (α) measurement results are presented in Figure 6. $\alpha(T)$ data between 300 K and 600 K show p-type temperature dependence, a highest measured α value of around 48 μV/K, and a room temperature α value of around 24 μV/K. The dependence is roughly linear, with the small drops at 440 and 580 K, both likely being a data artifacts. The positive α suggests holes as the majority charge carrier. Presumably, the α_{max} is higher than the measured maximum, but measurement at higher temperatures is required to precisely determine it.

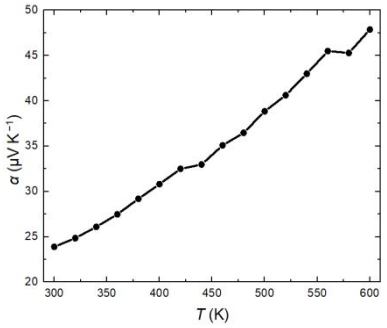

Figure 6. Temperature dependence of the Seebeck coefficient for $Yb_{10}Zn_6Sb_{12}$ single crystals.

Resistivity measurements were hampered by the small crystal size and proper estimation of the geometric factor. The values of the resistivity start at around 0.7 mΩ cm at 300 K and go to under 0.2 mΩ cm at around 440 K. The low resistivity is comparable with the resistivity of other Yb–Zn–Sb phases[49,50], and indicates weak metalicity. The shape of the curve (Figure S4), however, suggests $Yb_{10}Zn_6Sb_{12}$ to be a semiconductor, which is not entirely consistent with the electronic structure calculations (recall, done on a model $Yb_{10}Zn_8Sb_{12}$) but agreeing well with the electron count based on the Zintl concept. Since the temperature range is rather limited and the data shows much scatter, it is possible that the true nature of $\rho(T)$ is not revealed here, which calls for further and more comprehensive studies.

Conclusions

Two new ternary transition-metal-containing Zintl phases have been synthesized, and their structures determined using single-crystal X-ray diffraction. Both $Yb_{10}Zn_6Sb_{12}$ and $Eu_{10}Mn_6Bi_{12}$ crystallize in the orthorhombic space group *Cmmm*. The structures feature intricate anionic substructure of layered nature, where transition-metal-centered tetrahedra are conjoined via common corners, as well as Sb–Sb and Bi–Bi homoatomic bonds, imparting channel-like characteristics of the overall structure. Besides the common to both structures occupational disorder on Zn and Mn sites, there is also pronounced structural disorder on Yb cation site in $Yb_{10}Zn_6Sb_{12}$. The electron counts in both cases adhere to the valence rules (Zintl concept), and both phases can be reasonably classified as semiconductors, though $Yb_{10}Zn_6Sb_{12}$ appears to have some weakly semi-metallic properties.

These new compounds add to the knowledge base of Zintl antimonides and bismuthides and greatly increase the number of solids crystallizing in the respective structure type, $Eu_{10}Cd_6Bi_{12}$. Along these lines, expansion of the structural series seems possible, at least with analogous phases, like the hitherto unknown $Ca_{10}Zn_6Sb_{12}$, and the identification of these new phases is eagerly anticipated.

Author Contributions

Ryan Janzen: Investigation, Methodology, Formal analysis, Visualization, Writing - original draft.

Sviatoslav Baranets: Conceptualization, Investigation, Formal analysis, Writing - review & editing.

Svilen Bobev: Conceptualization, Supervision, Project administration, Writing - review & editing.

Conflicts of interest

There are no conflicts to declare.

Acknowledgements

This work was supported by the U.S. Department of Energy, Office of Science, Basic Energy Sciences through grant DE-SC0008885.

Notes and references

1 R. Nesper, *Angew. Chem. Int. Ed. Engl.*, 1991, **30**, 789–817.
2 E. Zintl, *Angew. Chem.*, 1939, **52**, 1–6.
3 W. Klemm, *Angew. Chem.*, 1950, **62**, 133–142.
4 K.-F. Liu and S.-Q. Xia, *J. Solid State Chem.*, 2019, **270**, 252–264.
5 P. Ren, Y. Liu, J. He, T. Lv, J. Gao and G. Xu, *Inorg. Chem. Front.*, 2018, **5**, 2380–2398.
6 S. M. Kauzlarich, S. R. Brown and G. J. Snyder, *Dalton Trans.*, 2007, 2099.
7 F. Gascoin, S. Ottensmann, D. Stark, S. M. Haïle and G. J. Snyder, *Adv. Funct. Mater.*, 2005, **15**, 1860–1864.
8 A. Ovchinnikov and S. Bobev, *J. Solid State Chem.*, 2019, **270**, 346–359.
9 G. S. Pomrehn, A. Zevalkink, W. G. Zeier, A. van de Walle and G. J. Snyder, *Angew. Chem. Int. Ed.*, 2014, **53**, 3422–3426.
10 Y. Wang and S. Bobev, *Chem. Mater.*, 2018, **30**, 3518–3527.
11 J. Y. Chan, S. M. Kauzlarich, P. Klavins, R. N. Shelton and D. J. Webb, *Chem. Mater.*, 1997, **9**, 3132–3135.
12 S. Baranets, A. Ovchinnikov and S. Bobev, in *Handbook on the Physics and Chemistry of Rare Earths*, eds. J.-C. G. Bünzli and V. K. Pecharsky, Elsevier, 2021, vol. 60, pp. 227–324.
13 E. Brechtel, G. Cordier and H. Schäfer, *Z. Naturforsch. B*, 1979, **34**, 1229–1233.
14 S.-Q. Xia and S. Bobev, *Inorg. Chem.*, 2007, **46**, 874–883.
15 S. M. Kauzlarich, T. Y. Kuromoto and M. M. Olmstead, *J. Am. Chem. Soc.*, 1989, **111**, 8041–8042.
16 S. Bobev, J. Merz, A. Lima, V. Fritsch, J. D. Thompson, J. L. Sarrao, M. Gillessen and R. Dronskowski, *Inorg. Chem.*, 2006, **45**, 4047–4054.
17 A. Ovchinnikov, B. Saparov, S.-Q. Xia and S. Bobev, *Inorg. Chem.*, 2017, **56**, 12369–12378.
18 N.-T. Suen, Y. Wang and S. Bobev, *J. Solid State Chem.*, 2015, **227**, 204–211.
19 I. R. Fisher, S. L. Bud'ko, C. Song, P. C. Canfield, T. C. Ozawa and S. M. Kauzlarich, *Phys. Rev. Lett.*, 2000, **85**, 1120–1123.
20 A. Ovchinnikov, S. Chanakian, A. Zevalkink and S. Bobev, *Chem. Mater.*, 2021, **33**, 3172–3186.
21 S. Bobev, J. D. Thompson, J. L. Sarrao, M. M. Olmstead, H. Hope and S. M. Kauzlarich, *Inorg. Chem.*, 2004, **43**, 5044–5052.
22 A. F. May, M. A. McGuire, J. Ma, O. Delaire, A. Huq and R. Custelcean, *J. Appl. Phys.*, 2012, **111**, 033708.
23 S.-Q. Xia and S. Bobev, *Chem. Asian J.*, 2007, **2**, 619–624.
24 A. F. May, M. A. McGuire and B. C. Sales, *Phys. Rev. B*, 2014, **90**, 075109.
25 J. Y. Chan, M. E. Wang, A. Rehr, S. M. Kauzlarich and D. J. Webb, *Chem. Mater.*, 1997, **9**, 2131–2138.
26 A. Mar, in *Handbook on the Physics and Chemistry of Rare Earths*, eds. K. A. Gschneidner Jr. and V. K. Pecharsky, Elsevier, 2006, vol. 36, pp. 1–82
27 P. C. Canfield and Z. Fisk, *Phil. Mag. B*, 1992, **65**, 1117–1123.
28 *SMART and SAINT, Bruker AXS Inc., Madison, Wisconsin, USA, 2014*.
29 *SADABS, Bruker AXS Inc., Madison, Wisconsin, USA, 2014*.
30 O. V. Dolomanov, L. J. Bourhis, R. J. Gildea, J. a. K. Howard and H. Puschmann, *J Appl. Cryst.*, 2009, **42**, 339–341.
31 G. M. Sheldrick, *Acta Cryst. A*, 2015, **71**, 3–8.
32 G. M. Sheldrick, *Acta Cryst. C*, 2015, **71**, 3–8.
33 L. M. Gelato and E. Parthé, *J Appl Cryst*, 1987, **20**, 139–143.
34 O. Anderson and O. Jepsen, The Stuttgart TB-LMTO-ASA Program; Max-Planck-Institut für Festkörperforschung: Stuttgart, Germany 1999.
35 U. von Barth and L. Hedin, *J. Phys. C: Solid State Phys.*, 1972, **5**, 1629–1642.
36 R. Dronskowski and P. E. Blöchl, *J. Phys. Chem.*, 1993, **97**, 8617–8624.
37 K. Imasato, C. Fu, Y. Pan, M. Wood, J. J. Kuo, C. Felser and G. J. Snyder, *Adv. Mater.*, 2020, **32**, 1908218.
38 S. Baranets and S. Bobev, *J. Solid State Chem.*, 2021, **303**, 122467.
39 L. Xin, G. Li, G. Auffermann, H. Borrmann, W. Schnelle, J. Gooth, X. Zhao, T. Zhu, C. Felser and C. Fu, *Mater. Today Phys.*, 2018, **7**, 61–68
40 S. Baranets, A. Ovchinnikov and S. Bobev, *Inorg. Chem.*, 2021, **60**, 6702–6711.
41 A. P. Holm, S.-M. Park, C. L. Condron, M. M. Olmstead, H. Kim, P. Klavins, F. Grandjean, R. P. Hermann, G. J. Long, M. G. Kanatzidis, S. M. Kauzlarich and S.-J. Kim, *Inorg. Chem.*, 2003, **42**, 4660–4667.
42 B. Saparov, S. Bobev, A. Ozbay and E. R. Nowak, *J. Solid State Chem.*, 2008, **181**, 2690–2696.
43 S.-Q. Xia and S. Bobev, *J. Comput. Chem.*, 2008, **29**, 2125–2133.
44 P. Pyykkö and M. Atsumi, *Chem. Eur. J.*, 2009, **15**, 186–197.
45 S. Baranets and S. Bobev, *Mater. Today Adv.*, 2020, **7**, 100094.
46 S. Baranets, H. He and S. Bobev, *Acta Cryst. C*, 2018, **74**, 623–627.
47 L. Pauling, *J. Am. Chem. Soc.*, 1947, **69**, 542–553.
48 D. Sánchez-Portal, R. M. Martin, S. M. Kauzlarich and W. E. Pickett, *Phys. Rev. B*, 2002, **65**, 144414.
49 E. L. Kunz Wille, N. S. Grewal, S. K. Bux and S. M. Kauzlarich, *Materials (Basel)*, 2019, **12**, 731.
50 O. Ya. Zelinska, A. V. Tkachuk, A. P. Grosvenor and A. Mar, *Chem. Met. Alloys*, 2008, **1**, 204–209.